IX CONGRESSO BRASILEIRO DE
ENGENHARIA E CIÊNCIAS TÉRMICAS
9th BRAZILIAN CONGRESS OF THERMAL
ENGINEERING AND SCIENCES

Paper CIT02-0340

THREE DIMENSIONAL FINITE VOLUME FLOW SIMULATIONS USING UNSTRUCTURED MESHES

Leonardo Costa Scalabrin
Instituto Tecnológico de Aeronáutica
CTA/ITA/IEAA
12228-900 - São José dos Campos - SP, Brazil
scala@iae.cta.br

João Luiz F. Azevedo
Instituto de Aeronáutica e Espaço
CTA/IAE/ASE-N
12228-904 - São José dos Campos - SP, Brazil
azevedo@iae.cta.br

Abstract. *This paper will discuss the results obtained using a finite volume code with three dimensional unstructured grids to simulate inviscid and viscous flows. A fully explicit, 2nd-order accurate, 5-stage, Runge-Kutta time stepping scheme was used to perform the time march of the flow equations. Two different forms for flux calculation on the volume faces were implemented. The first one is a centered scheme which requires the addition of artificial dissipation terms. The other form for flux calculation is based on the flux vector splitting technique. The 1st-order Van Leer scheme was implemented. The boundary conditions are set using Riemann invariants. The implementation uses a cell centered, face-based data structure. The paper will present the first simulation results obtained for the Brazilian Satellite Launcher (VLS). The simulations were performed for supersonic and transonic inviscid flows and for supersonic viscous flows over the vehicle at zero angle-of-attack .*

Keywords: *Aerodynamics, numerical methods, computational fluid dynamics, finite volume technique, launch vehicles.*

1. Introduction

Many approaches have been developed to simulate aerodynamic flows over three-dimensional aerodynamic configurations. The Computational Fluid Dynamics group at IAE already achieved good results using finite differences techniques on structured grids and finite element techniques on unstructured grids. This paper will discuss the results obtained so far using a finite volume technique on three dimensional unstructured grids to simulate inviscid and viscous flows.

A fully explicit, 2nd-order accurate, 5-stage, Runge-Kutta time stepping scheme was used to perform the time march of the flow equations. Two different forms for flux calculation on the volume faces were implemented. The first one is the centered scheme which requires the addition of an artificial dissipation term. In this work, the dissipation terms proposed by Jameson and his co-authors (Jameson et al., 1981) were used. The other form for flux calculation is based on the flux vector splitting technique. The 1st-order Van Leer scheme (Van Leer, 1982; Anderson et al., 1986) was implemented. The boundary conditions are set using Riemann invariants. The implementation uses a cell centered, face-based data structure.

The paper will present the first simulation results obtained for the Brazilian Satellite Launcher (VLS) using the code newly developed. Inviscid transonic and supersonic flows over the VLS first stage flight configuration at zero angle-of-attack were simulated as well as viscous supersonic flow over the VLS second stage flight configuration at zero angle-of-attack. The numerical results are qualitatively satisfactory and present the aerodynamic features verified in experimental tests.

2. Theoretical Formulation

2.1. General Formulation

The long term objective of the Computational Fluid Dynamics group at IAE is to develop the capability to simulate three-dimensional, compressible, viscous turbulent flows over general launch vehicle configurations. The present paper discusses the progress attained in the simulation of three dimensional compressible viscous laminar flows using a finite volume approach. In this case, the flow can be modeled by the Navier-Stokes

equations. These equations are the more general formulation for flows for which the continuum hypothesis can be assumed. The Navier-Stokes equations, for a perfect gas, can be written as

$$\frac{\partial Q}{\partial t} + \frac{\partial \left(E_e - E_v\right)}{\partial x} + \frac{\partial \left(F_e - F_v\right)}{\partial y} + \frac{\partial \left(G_e - G_v\right)}{\partial z} = 0 \quad , \tag{1}$$

where Q is the dimensionless vector of conserved variables, defined as

$$Q = \left[\begin{array}{cccccc} \rho & \rho\, u & \rho\, v & \rho\, w & e \end{array} \right] \quad , \tag{2}$$

where ρ is the fluid density, u, v and w are the Cartesian velocity components and e is the fluid total energy. In this work, all the variables are non-dimensionalized according to the work of Long et al., 1991. The E_e, F_e and G_e terms are the dimensionless inviscid flux vectors and E_v, F_v and G_v are the dimensionless viscous flux vectors. The E_e, F_e and G_e vectors are given by

$$E_e = \left\{ \begin{array}{c} \rho\, u \\ \rho\, u^2 + p \\ \rho\, u\, v \\ \rho\, u\, w \\ (e+p)\, u \end{array} \right\} \quad , \quad F_e = \left\{ \begin{array}{c} \rho\, v \\ \rho\, v\, u \\ \rho\, v^2 + p \\ \rho\, v\, w \\ (e+p)\, v \end{array} \right\} \quad , \quad G_e = \left\{ \begin{array}{c} \rho\, w \\ \rho\, w\, u \\ \rho\, w\, v \\ \rho\, w^2 + p \\ (e+p)\, w \end{array} \right\} \quad . \tag{3}$$

The viscous flux vectors can be written as

$$E_v = \frac{1}{Re} \left\{ \begin{array}{c} 0 \\ \tau_{xx} \\ \tau_{xy} \\ \tau_{xz} \\ \tau_{xx}\, u + \tau_{xy}\, v + \tau_{xz}\, w + \frac{\gamma \mu}{Pr} \frac{\partial e_i}{\partial x} \end{array} \right\} \quad , \quad F_v = \frac{1}{Re} \left\{ \begin{array}{c} 0 \\ \tau_{xy} \\ \tau_{yy} \\ \tau_{yz} \\ \tau_{xy}\, u + \tau_{yy}\, v + \tau_{yz}\, w + \frac{\gamma \mu}{Pr} \frac{\partial e_i}{\partial x} \end{array} \right\} \quad ,$$

$$G_v = \frac{1}{Re} \left\{ \begin{array}{c} 0 \\ \tau_{xz} \\ \tau_{yz} \\ \tau_{zz} \\ \tau_{xz}\, u + \tau_{yz}\, v + \tau_{zz}\, w + \frac{\gamma \mu}{Pr} \frac{\partial e_i}{\partial x} \end{array} \right\} \quad , \tag{4}$$

where $Re = \frac{\rho\, |\vec{v}|\, \ell}{\mu}$ is the Reynolds number, $Pr = \frac{\mu\, \mathrm{Cp}}{\kappa}$ is the Prandtl number, μ is the molecular viscosity coefficient of the fluid, Cp is the specific heat at constant pressure, κ is the thermal conductivity coefficient and ℓ is the characteristic length of the problem. In the previous equations, the dimensionless pressure, p, can be calculated from the perfect gases equation as

$$p = (\gamma - 1) \left[e - \frac{1}{2} \rho \left(u^2 + v^2 + w^2 \right) \right] \quad . \tag{5}$$

One should observe that the Euler equations are obtained from the Navier-Stokes equations as Re approaches infinity.

The finite volume technique was used to obtain the solution of the Navier-Stokes equations. The formulation of the method is obtained by an integration of the flow equations in a finite volume. The application of Gauss theorem for each finite volume yields

$$\int_{V_i} \frac{\partial Q}{\partial t}\, dV + \int_{S_i} \left(\left(E_e - E_v\right) \vec{i} + \left(F_e - F_v\right) \vec{j} + \left(G_e - G_v\right) \vec{k} \right) \cdot d\vec{S} = 0 \quad , \tag{6}$$

where $d\vec{S}$ is the outward oriented normal area vector. It should be noted that the vector is outward in relation to the i-th element. Defining the mean value for the conserved variables in the volume as

$$Q_i = \frac{1}{V_i} \int_{V_i} Q\, dV_i \quad , \tag{7}$$

the final form of the finite volume formulation for the Navier-Stokes equations can be written for an elementary volume as

$$\frac{\partial Q_i}{\partial t} = -\frac{1}{V_i} \sum_{k=1}^{nf} \left(\left(E_{ek} - E_{vk}\right) \vec{i} + \left(F_{ek} - F_{vk}\right) \vec{j} + \left(G_{ek} - G_{vk}\right) \vec{k} \right) \cdot \vec{S}_k \quad , \tag{8}$$

where nf is the number of faces which forms the element and $\vec{S}_k$ is the outward oriented normal area vector of the k-th face. As before, the vector is outward in relation to the i-th element. The code developed is able to

simulate flows on grids constituted of tetrahedra, hexahedra, triangular base prisms, square base pyramids or a mix of these types of elements. The previous equation also indicates that the integral was discretized assuming the fluxes to be constant on the faces. In order to solve Eq. (8), Jameson's method was implemented (Jameson et al., 1981). Furthermore, the flux vector splitting proposed by Van Leer (Van Leer, 1982; Anderson et al., 1986) was implemented as an alternative for the flux calculation on the faces for flows at high Mach numbers.

2.2. Jameson's Method

The integration in time of Eq. (8) can be written using a 5-stage Runge-Kutta type scheme as

$$\begin{aligned} Q_i^{(0)} &= Q_i^n \quad , \\ Q_i^{(\ell)} &= Q_i^{(0)} - \frac{\alpha_\ell \, \Delta t_i}{V_i} \left[C\left(Q_i^{(\ell-1)}\right) - V\left(Q_i^{(\ell-1)}\right) - D\left(Q_i^{\left(\ell'\right)}\right) \right] \quad \ell = 1, \cdots, 5 \quad , \\ Q_i^{n+1} &= Q_i^{(5)} \quad . \end{aligned} \tag{9}$$

In the previous equations, $C\left(Q_i\right)$ is the convective operator calculated for the i-th control volume. This operator is calculated as the sum of the fluxes on the faces which constitute the volume, or, mathematically

$$C\left(Q_i\right) = \sum_{k=1}^{nf} \left[E_e\left(Q_k\right) \vec{i} + F_e\left(Q_k\right) \vec{j} + G_e\left(Q_k\right) \vec{k} \right] \cdot \vec{S}_k \quad , \tag{10}$$

where Q_k is defined as

$$Q_k = \frac{Q_m + Q_i}{2} \quad . \tag{11}$$

Q_m and Q_i are the conserved properties in the volumes at each side of the k-th face and m indicates the neighbor of the i-th element. $V\left(Q_i\right)$ is the viscous operator calculated for the i-th control volume. This operator is the sum of the viscous fluxes on the faces which constitute the volume, calculated as

$$V\left(Q_i\right) = \sum_{k=1}^{nf} \left[E_v\left(Q_k\right) \vec{i} + F_v\left(Q_k\right) \vec{j} + G_v\left(Q_k\right) \vec{k} \right] \cdot \vec{S}_k \quad . \tag{12}$$

In this case, both the conserved variable vector and the derivatives on the face, used to compute the viscous terms, are calculated as the arithmetic average between these quantities in the two volumes which contain the face. The coefficients α_ℓ are $1/4$, $1/6$, $3/8$, $1/2$ e 1 for $\ell = 1, \cdots, 5$, respectively. The ℓ' superscript indicates that the artificial dissipation term is calculated only on the first, third and fifth stages. For the inviscid calculations, the artificial dissipation term is calculated in the first and in the second stages.

The artificial dissipation operator, $D\left(Q_i\right)$, is calculated according to the ideas developed by Jameson and co-authors (Jameson et al., 1981). The operator is very similar to the one proposed by Mavriplis (Mavriplis, 1988; Mavriplis, 1990). The operator used is built by the undivided Laplacian and bi-harmonic operators. In regions where the properties gradients are high, the bi-harmonic operator is turned off in order to avoid oscillations. In smooth regions, the undivided Laplacian operator is turned off. A numerical pressure sensor is responsible for this switching between the operators. The expression for the Jameson artificial dissipation terms is given by

$$D\left(Q_i\right) = \sum_{m=1}^{nv} \left\{ \left(\frac{A_m + A_i}{2} \right) \left[\epsilon_2 \left(Q_m - Q_i\right) + \epsilon_4 \left(\nabla^2 Q_m - \nabla^2 Q_i \right) \right] \right\} \quad , \tag{13}$$

where m represents the neighbors of the i-th element and nv is the total number of neighbors of the i-th element. The undivided harmonic operator and the A_i coefficients can be written as

$$\nabla^2 Q_i = \sum_{m=1}^{nv} \left[Q_m - Q_i \right] \quad \text{e} \quad A_i = \frac{V_i}{\Delta t_i} \quad . \tag{14}$$

The ϵ factors are based on the pressure sensor. The numerical pressure sensor can be calculated as

$$\nu_s = \frac{\sum_{m=1}^{nv} \left| p_m - p_i \right|}{\sum_{m=1}^{nv} \left[p_m + p_i \right]} \quad , \quad \epsilon_2 = \frac{1}{2} \max\left(\nu_{s_i}, \nu_{s_m}\right) \quad \text{e} \quad \epsilon_4 = \max\left(0, \frac{3}{256} - \epsilon_2\right) \quad . \tag{15}$$

The time step for each volume, Δt_i, is calculated using the CFL number. Hence,

$$\Delta t_i = \frac{\text{CFL} \; \ell_i}{\left(\left| \vec{v_i} \right| + a_i \right)} \quad , \tag{16}$$

where a_i is the speed of sound in the i-th element, $\left| \vec{v_i} \right|$ is the magnitude of the flow velocity in the i-th element and ℓ_i is the characteristic length of the element. The characteristic length was set as the smallest distance between the element centroid and the centroids of each face that forms the element.

2.3. Van Leer's Flux Vector Splitting Technique

It can be shown that spatial discretization schemes which follow the information propagation direction are naturally dissipative. Hence, the utilization of this type of schemes eliminates the need of externally added artificial dissipation terms to the numerical method. This line of research started with the work of Steger and Warming (Steger and Warming, 1981). In that work, the flux vectors are splitted using the homogeneous property of the Euler equations and the signs of the eigenvalues of the flux Jacobian matrices. Then, each part of the flux is differenced according to its own propagation direction. This technique was vastly used but it presented problems at sonic points (Steger and Warming, 1981). This problem is related to the abrupt change in the direction of propagation and, consequently, of the eigenvalues that occurs at sonic points, causing some oscillation in the results. Van Leer (Van Leer, 1982; Anderson et al., 1986) proposed another way of splitting the fluxes which is continuously differentiable and, consequently, smoother at sonic points. The final form of Van Leer's flux vectors is presented below for the x component.

The flux vector splitting is given by

$$\begin{aligned} E_e^+ &= E_e \quad , \quad E_e^- = 0 \quad \text{for} \quad M_x \geq 1 \\ E_e^+ &= 0 \quad , \quad E_e^- = E_e \quad \text{for} \quad M_x \leq -1 \quad , \end{aligned} \tag{17}$$

and for subsonic flow, $|M_x| \leq 1$,

$$E^{\pm} = \left\{ \begin{array}{c} f_1^{\pm} \\ f_1^{\pm} \left[(\gamma - 1) \pm 2\, a \right] / \gamma \\ f_1^{\pm}\, v \\ f_1^{\pm}\, w \\ f_1^{\pm} \left[\left\{ (\gamma - 1)\, u \pm 2\, a \right\}^2 / \left\{ 2\, \left(\gamma^2 - 1 \right) \right\} + v^2/2 + w^2/2 \right] \end{array} \right\} \quad , \tag{18}$$

where

$$f_1^{\pm} = \pm\, a\, \left[1/2\, (M_x \pm 1) \right]^2 \quad \text{and} \quad M_x = \frac{u}{a} \quad . \tag{19}$$

In the previous equations, the superscript $\pm$ refers to the orientation of propagation of the flux, i.e., $+$ to the flux with the same orientation of the x axis and $-$ to the flux with the orientation contrary to the x axis.

The convective operator on a face can be mounted by summing the flux vectors of the volumes which contain the face. This have to take in account the position of the volumes relative to the face in order to sum the correct flux part, i.e., E^+ or E^-. Remembering that $\vec{S}_k$ is the outward oriented normal area vector of the k-th face and that the vector is outward in relation to the i-th volume, the expressions for the x-component flux on a face are given by:

For $S_{k_x} > 0$

$$E_k = E_e^+ \left(Q_i \right) + E_e^- \left(Q_{nb} \right) \quad , \tag{20}$$

and for $S_{k_x} < 0$

$$E_k = E_e^- \left(Q_i \right) + E_e^+ \left(Q_{nb} \right) \quad , \tag{21}$$

where S_{k_x} is the x component of the outward oriented normal area vector, $\vec{S}_k$. The expression for the fluxes in the y and z directions are easily induced from the expressions presented in this paper. Finally, the expression for the convective operator in the i-th volume is

$$C\left(Q_i \right) = \sum_{k=1}^{nf} \left[E_k\, \vec{i} + F_k\, \vec{j} + G_k\, \vec{k} \right] \cdot \vec{S}_k \quad . \tag{22}$$

Further details in the implementation of the Van Leer's flux vector splitting technique can be seen in Azevedo and Korzenowski, 1998.

2.4. Boundary Conditions

"Ghost" volumes were used in order to enforce the boundary conditions. The boundary conditions for external flow implemented in the three dimensional finite volume code were wall, for viscous and inviscid flows, farfield, symmetry and supersonic exit conditions.

The wall boundary conditions for inviscid flows require the velocity component normal to the wall to be equal to zero. An auxiliary coordinate system is used in order to set this boundary condition. One of its axis is taken aligned to the normal vector to the face. This axis is called $\vec{n}$. One of the other axis is taken tangent to

the face. This axis is called $\vec{t}$. The third axis is obtained from the cross product of the two other axis and it is called $\vec{r}$. The velocity of the element internal to the boundary, in the Cartesian coordinate system, is given by

$$\vec{v_0} = \left[u\,\vec{i} + v\,\vec{j} + w\,\vec{k} \right] \quad . \tag{23}$$

The projections of this velocity vector in the auxiliary coordinate system are

$$\begin{aligned} v_{0n} &= \vec{v}_0 \cdot \vec{n} = u\,n_x + v\,n_y + w\,n_z \\ v_{0t} &= \vec{v}_0 \cdot \vec{t} = u\,t_x + v\,t_y + w\,t_z \\ v_{0r} &= \vec{v}_0 \cdot \vec{r} = u\,r_x + v\,r_y + w\,r_z \quad . \end{aligned} \tag{24}$$

The velocity in the "ghost" element must be set in a way that, when summed to the internal element, the resultant normal component is equal to zero. Hence, the velocity components in the "ghost" element, indicated by the subscript g, in the auxiliary coordinate system, must be

$$v_{\mathrm{g}n} = -v_{0n} \quad , \quad v_{\mathrm{g}t} = v_{0t} \quad , \quad v_{\mathrm{g}r} = v_{0r} \quad , \tag{25}$$

and the velocity in the "ghost" element, in the auxiliary coordinate system, is

$$\vec{v}_{\mathrm{g}} = v_{\mathrm{g}n}\,\vec{n} + v_{\mathrm{g}t}\,\vec{t} + v_{\mathrm{g}r}\,\vec{r} \quad . \tag{26}$$

The vectors $\vec{n}$, $\vec{t}$ and $\vec{r}$ can be written in terms of its Cartesian components $\vec{i}$, $\vec{j}$ e $\vec{k}$. Then, it can be obtained that the Cartesian velocity components in the "ghost" volume, which satisfy the boundary condition on the face, are

$$\vec{v}_{\mathrm{g}} = \left(v_{\mathrm{g}n}\,n_x + v_{\mathrm{g}t}\,t_x + v_{\mathrm{g}r}\,r_x \right)\,\vec{i} + \left(v_{\mathrm{g}n}\,n_y + v_{\mathrm{g}t}\,t_y + v_{\mathrm{g}r}\,r_y \right)\,\vec{j} + \left(v_{\mathrm{g}n}\,n_z + v_{\mathrm{g}t}\,t_z + v_{\mathrm{g}r}\,r_z \right)\,\vec{k} \quad . \tag{27}$$

The other properties in the "ghost" volume are

$$\rho_g = \rho_0 \quad \text{and} \quad e_g = e_0 \quad . \tag{28}$$

The symmetry boundary conditions are implemented precisely in the same fashion as the boundary conditions for a wall in inviscid flow.

The wall boundary conditions for viscous flows are simpler. In this case, the properties in the "ghost" element must be set in a way that the velocity in the face is equal to zero. Hence, the velocity components in the "ghost" volumes must be

$$v_{\mathrm{g}x} = -v_{0x} = -u \quad , \quad v_{\mathrm{g}y} = -v_{0y} = -v \quad , \quad v_{\mathrm{g}z} = -v_{0z} = -w \quad , \tag{29}$$

or

$$\vec{v_g} = \left[-u\,\vec{i} - v\,\vec{j} - w\,\vec{k} \right] \quad . \tag{30}$$

As in the inviscid flow case, the density and the total energy in the "ghost" element are set equal to their corresponding values in the internal volume.

Another boundary condition implemented in the code was the farfield condition. Riemman invariants were used in order to correctly set the properties values on the boundary face. The Riemman invariants are derived from the characteristic relations which relate properties between the two sides of the faces. The expressions involved in the calculations are

$$R^- = R^-_\infty = q_{\infty n} - \frac{2}{\gamma - 1}\,a_\infty \quad , \quad R^+ = R^+_e = q_{en} + \frac{2}{\gamma - 1}\,a_e \quad , \tag{31}$$

where $q_{\infty n} = \vec{q}_\infty \cdot \vec{n}$, $q_{en} = \vec{q}_e \cdot \vec{n}$ and $\vec{n}$ is the unit outward normal vector. Resolving for q_n and a, one can obtain that

$$q_{fn} = \frac{R^+_e + R^-_\infty}{2} \quad , \quad a_f = \left(\frac{\gamma - 1}{4} \right) \left(R^+_e - R^-_\infty \right) \quad . \tag{32}$$

For a subsonic exit boundary, $M_e = |\vec{v}_e| / a_e < 1$, the velocities components are

$$\begin{aligned} u_f &= u_e + (q_{fn} - q_{en})\,n_x \quad , \\ v_f &= v_e + (q_{fn} - q_{en})\,n_y \quad , \\ w_f &= w_e + (q_{fn} - q_{en})\,n_z \quad . \end{aligned} \tag{33}$$

Note that this equation relates the velocity components in the internal element with the boundary face velocity components. The difference between these components are caused by the properties jump between q_{fn} and q_{ne}.

The other flow properties will be obtained from an extrapolation of the entropy of the internal element, which yields

$$\rho_f = \left(\frac{\rho_e^\gamma \, a_f^2}{\gamma \, p_e} \right)^{\frac{1}{\gamma - 1}} \quad . \tag{34}$$

For a supersonic exit boundary, $M_e = |\vec{v}_e| / a_e > 1$, the velocity components and the density must be extrapolated from the domain, i.e.,

$$\rho_f = \rho_e \quad , \quad u_f = u_e \quad , \quad v_f = v_e \quad , \quad w_f = w_e \quad , \quad e_f = e_e \quad . \tag{35}$$

For a subsonic entrance boundary, $M_e = |\vec{v}_e| / a_e < 1$, the velocity components are calculated as

$$\begin{aligned} u_f &= u_\infty + (q_{fn} - q_{\infty n}) \, n_x \quad , \\ v_f &= v_\infty + (q_{fn} - q_{\infty n}) \, n_y \quad , \\ w_f &= w_\infty + (q_{fn} - q_{\infty n}) \, n_z \quad , \end{aligned} \tag{36}$$

and the entropy of the farfield flow is extrapolated to the boundary, which yields

$$\rho_f = \left(\frac{\rho_\infty^\gamma \, a_f^2}{\gamma \, p_\infty} \right)^{\frac{1}{\gamma - 1}} \quad . \tag{37}$$

For a supersonic entrance boundary, $M_e = |\vec{v}_e| / a_e > 1$, the velocity components and the density must be extrapolated from the farfield flow, i.e,

$$\rho_f = \rho_\infty \quad , \quad u_f = u_\infty \quad , \quad v_f = v_\infty \quad , \quad w_f = w_\infty \quad , \quad e_f = e_\infty \quad . \tag{38}$$

It must be noted that all the expressions derived for the Riemann Invariants calculate the flow properties on the face. However, for the implementation of the boundary conditions, one has to obtain the flow properties in the "ghost" volumes. From Eq. (11), the expression for the conserved properties in the "ghost" volume is

$$Q_g = 2 \, Q_f - Q_e \quad , \tag{39}$$

where Q_g is the conserved property vector in the "ghost" volume, Q_f is the conserved property vector on the face and Q_e is the conserved property vector in the internal element.

Problems were detected when applying farfield conditions to exit boundaries in supersonic viscous flow. The code was presenting convergence problems and sometimes, even, diverging. Previous experience in the group relates this problem to a inconsistent treatment of boundary faces inside and outside the boundary layer. The farfield boundary condition detects supersonic flow outside the boundary layer and, then, extrapolates the values from the domain to the "ghost" volume. However, inside the boundary layer, the farfield boundary condition detects subsonic flow and the properties in the "ghost" volume are calculated using Riemann invariants. This different treatment on the boundary causes pressure gradients in the boundary layer, which is inconsistent to the classical boundary layer theory, and it gives rise to convergence problems. To solve this problem, a supersonic exit boundary condition for viscous flow was implemented. This type of boundary condition forces the properties of the domain to be extrapolated to the "ghost" volumes. Therefore, it should be used only when the user is sure that the flow is supersonic at the exit boundary.

3. Results and Discussion

In order to test the code, aerodynamic flows over the VLS were simulated. The inviscid flows over the VLS in its take-off configuration were simulated for zero angle-of-attack and freestream Mach numbers $M = 2.0$ and $M = 0.9$. These flight conditions were chosen considering the dominant supersonic characteristic of the vehicle flight and the numerical difficulties that arise at transonic simulations. In addition, the viscous flow over the VLS central body for zero angle-of-attack and $M = 2.0$ was simulated. This section presents the results obtained.

3.1. Inviscid Flow Simulation over the VLS for $M_\infty = 2.0$ and Zero Angle-of-attack

A general view of the three-dimensional mesh used in this simulation is presented in Fig. (1). This tetrahedral mesh has approximately 106,000 nodes and 581,000 volumes. The geometry simulated did not include the engine nozzles, as this part of the geometry cannot be adequately simulated with an inviscid model (Strauss and Azevedo, 1999). A closer view of the rocket nose can be observed in Fig. (2(a)) and a closer view of the booster nose cap is in Fig. (2(b)). These figures present only one longitudinal plane of the mesh. Despite its

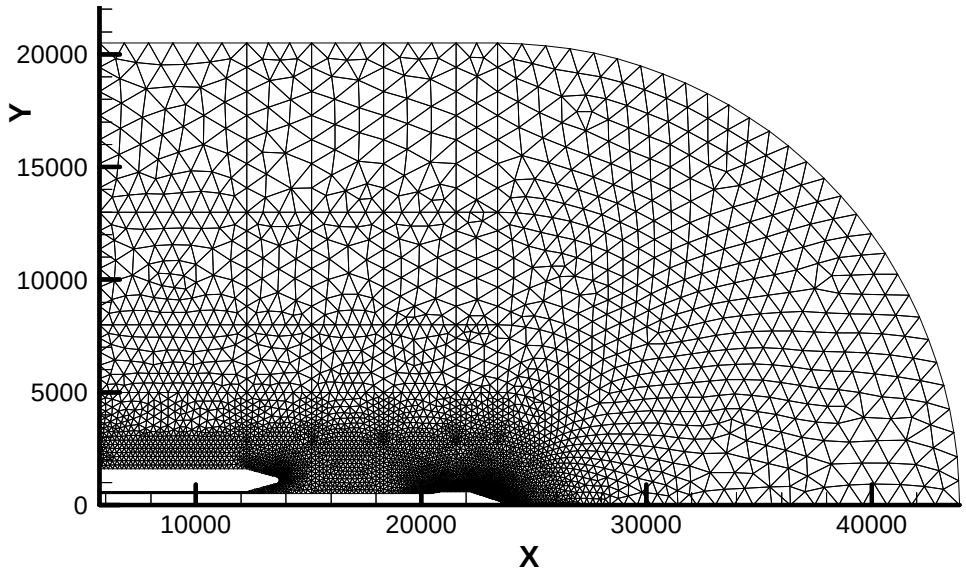

Figure 1: Overview of the mesh over the VLS first stage flight configuration.

size, the mesh is not refined enough near the body, as one can see in Fig. (2). In addition, the mesh wastes points near the boundaries, as clearly indicated in Fig. (1). However, as this was the first test of the code, the authors did not opted to correct the mesh problems.

Figure (3) shows the density contours over the domain. One can observe the detached shock waves in front of the rocket nose and in front of the boosters. A high pressure zone between the boosters, created by shock wave reflections, is also highlighted by this figure. This high pressure zone can be more detailed observed in

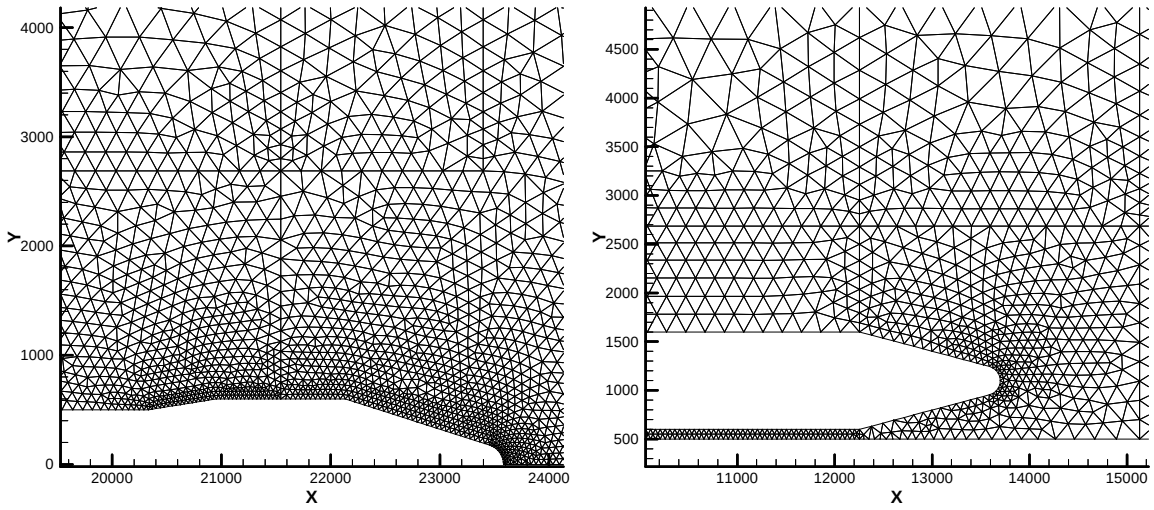

(a) Mesh near the central body forebody.

(b) Mesh near the booster nose cap.

Figure 2: Detailed view of the mesh.

Fig. (4(a)), which also shows a very low pressure region after the high pressure region. This low pressure region is originated by the outward deflection of the flow caused by the presence of the high pressure region. The flow in the vehicle forebody can be observed in Fig. (4(b)). This figure presents the detached shock wave and the stagnation region in front of the rocket. Furthermore, it also presents the expansion which occurs along the conical region and over the corners of the payload fairing and a shock wave over the end of the boattail.

Figure (5) presents the Mach number contours over the complete vehicle. The main features of the flow described using the density plots can also be observed in this picture, mainly the detached shock waves, the high and low speed regions near the boosters, the stagnation points and the expansion in the forebody region. A different feature observed in this figure is the presence of a layer near the body where the Mach number is

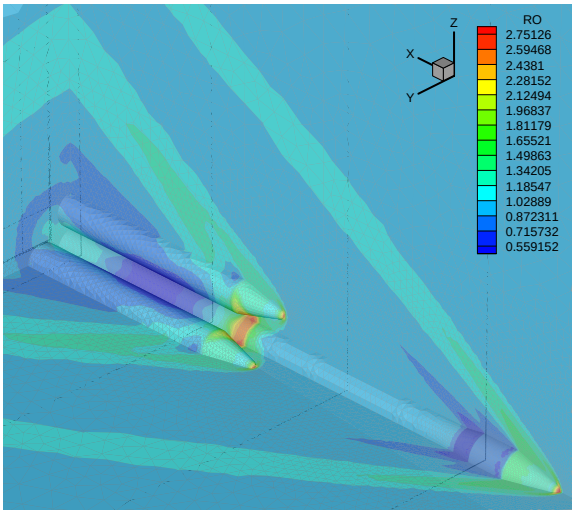

Figure 3: Density contours over the VLS for $M_\infty = 2.0$ and zero angle-of-attack.

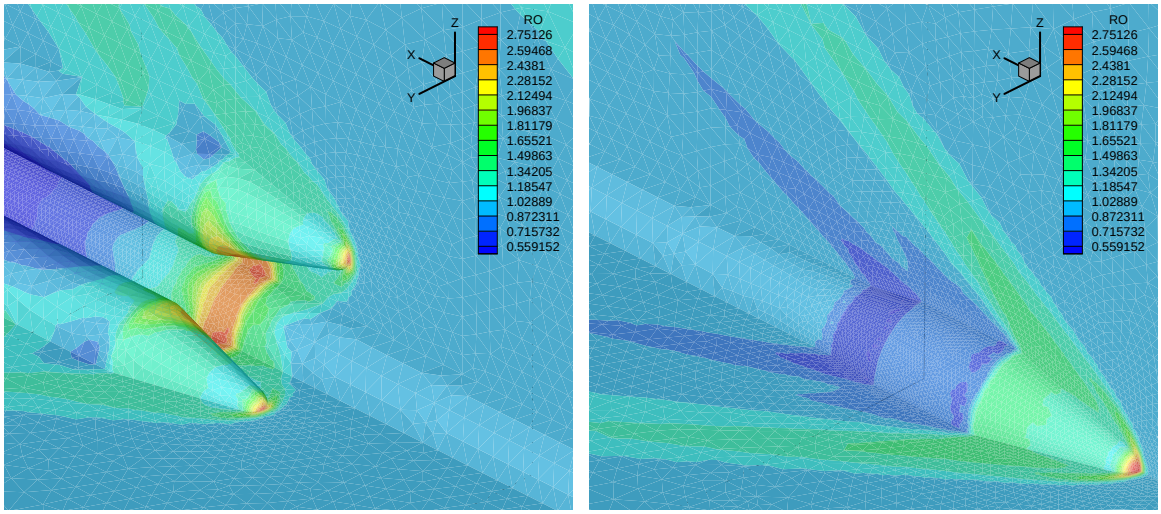

(a) Boosters nose cap region.

(b) Vehicle forebody region.

Figure 4: Detailed view of the density contours over the VLS for $M_\infty = 2.0$ and zero angle-of-attack.

lower than the freestream value. Over this cylindrical region, the Mach number is expected to be equal to the freestream Mach number. The authors believe that this problem is related to the pressure boundary conditions on the vehicle wall, as described in the scientific literature (Chakravarthy, 1983).

3.2. Inviscid Flow Simulation over the VLS for $M_\infty = 0.9$ and Zero Angle-of-attack

An overview of the flow over the VLS is presented in Fig. (6). The main features of the flow are clear in this figure. These are the stagnation points in front of the rocket nose and in front of the booster nose cap, the shock wave in the middle of the payload fairing and the shock waves over the boosters. Figure (7(a)) shows a more detailed view of the rocket forebody. In this figure, besides the stagnation point and the shock wave, one can see the expansions over the corners of the payload fairing and a small shock wave over the end of the boattail. The region near the booster nose cap can be better observed in Fig. (7(b)). In this figure, one can see that the flow rapidly accelerates between the boosters until it encounters a shock wave. It should be noted that, for this transonic case, there is no high pressure region as evident as in the supersonic case. In the supersonic case, the high pressure region was formed by the intense shock reflections in the region between the boosters.

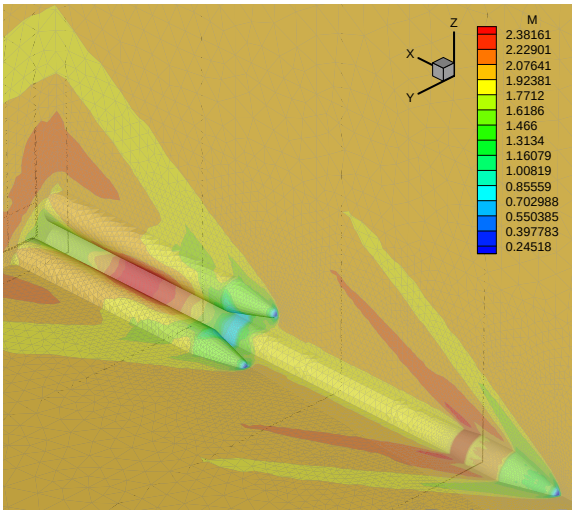

Figure 5: Mach number contours over the VLS for $M_\infty = 2.0$ and zero angle-of-attack.

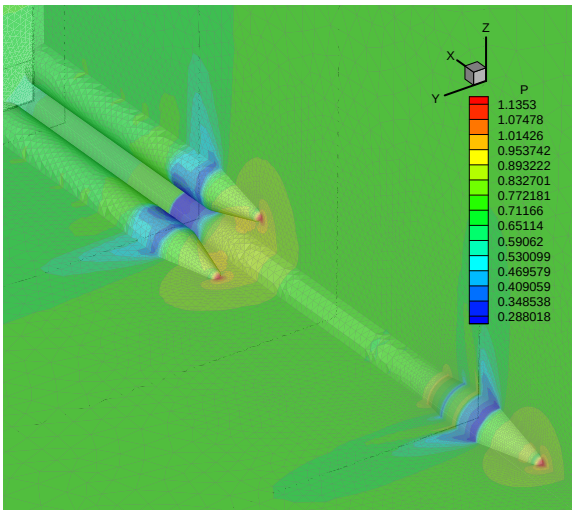

Figure 6: Pressure contours over the VLS for $M_\infty = 0.9$ and zero angle-of-attack.

3.3. Viscous Flow Simulation over the VLS for $M_\infty = 2.0$ and Zero Angle-of-attack

In order to start the tests with viscous flow simulations, the authors opted to simulate the VLS central body at $M_\infty = 2.0$ and zero angle-of-attack. This configuration was chosen because of the facility to generate an adequate mesh for viscous calculation. A hybrid mesh composed by hexahedra and prisms was generated. Hexahedral meshes can concentrate many volumes in the normal direction and save volumes in the other directions, which do not present relevant gradients. A view of the mesh over the vehicle forebody is presented in Fig. (8). The mesh is composed by 100,815 nodes and 89,280 volumes. It is evident the mesh refinement near the body, which is necessary to solve the viscous gradients. Figure (9) presents the Mach number contours near the rocket nose. The main characteristics of the flow are similar to the inviscid case, i.e., a detached shock wave, the expansions over the corners of the payload fairing and the shock wave over the end of the boattail. The blue color of the body indicates the velocity to be zero on the surface and the boundary layer is visible as a layer of yellow over the rocket. Clearly, the boundary layer increases its thickness along the cylindrical region of the vehicle. A pressure contour plot is presented in Fig. (10). In this figure, one can observe that the pressure does not vary in the boundary layer, as predicted by the classical boundary layer theory. Figures (11(a)) and (11(b)) show the velocity profiles over the vehicle nose and over the end of the boattail. The laminar characteristic of this simulation is clear because of the smooth variation of the velocity profiles.

4. Concluding Remarks

The paper presented the first results obtained with a finite volume code developed to solve the Euler and Navier-Stokes equations over complex aerodynamic bodies. The code uses a Runge-Kutta type scheme to

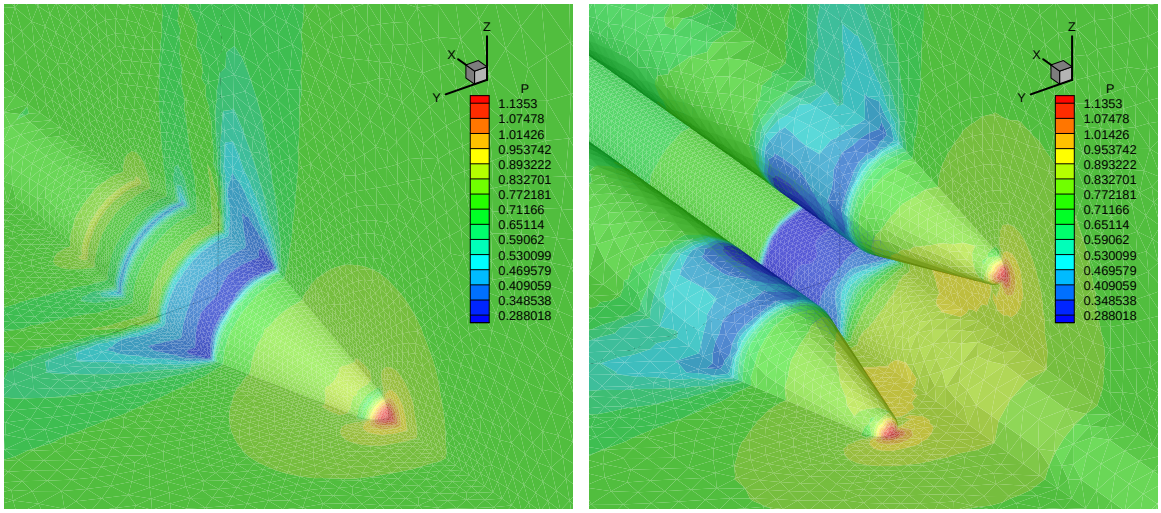

(a) Vehicle forebody region.

(b) Boosters nose cap region.

Figure 7: Detailed view of the pressure contours over the VLS for $M_\infty = 0.9$ and zero angle-of-attack.

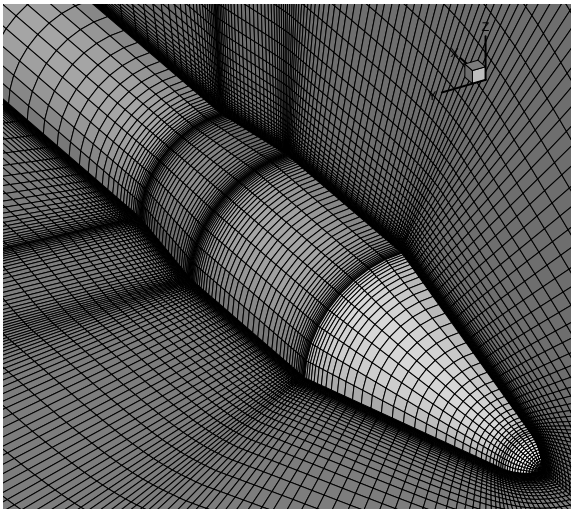

Figure 8: Mesh view near the VLS nose.

perform the time march. The code has two options to calculate the fluxes on the volume faces. The first one is the centered scheme proposed by Jameson and the second is based on the the flux vector splitting technique developed by Van Leer. The code is designed to use unstructured meshes composed by any combination of tetrahedra, hexahedra, prisms and pyramids.

The tests with the code for inviscid simulations yielded good results. For the supersonic case, the code solved for all the main features present in this type of flow, such as detached shock waves, stagnation points and expansions over corners. The code also predicted the high pressure region between the boosters originated from the various shock wave reflections in this region. However, more mesh refinement is needed in this region in order to capture all the reflections. The authors have implemented three-dimensional adaptive mesh refinement routines which will be applied to this problem in the future. For the transonic case, the code presented good results too. The code predicted the main features of the flow without the problems usually associated with transonic flow simulations. For instance, a previous work in the group with this test case and using the same mesh, presented several problems related to solution oscillations in the domain (Scalabrin et al., 2002). That code needed a more refined mesh to yield results with similar quality to the present ones.

The test for viscous flow simulation was also satisfactory. All the flow features were captured in the simulation, including the boundary layer. The boundary layer presented a laminar profile because the code does not have a turbulence model implemented yet. Despite the absence of comparisons between numerical and experimental results, the authors are confident in the potential of this new code. At the present moment, the

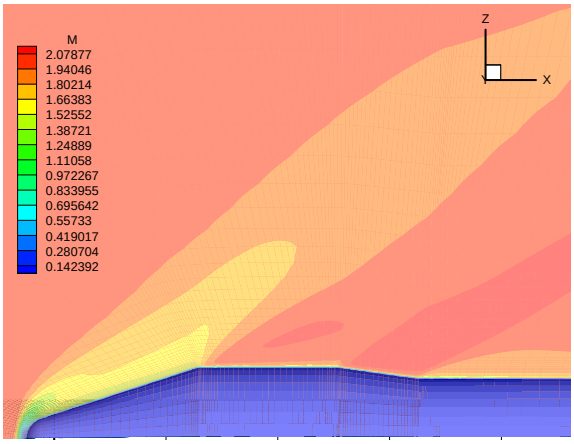

Figure 9: Mach number contours over the vehicle forebody for $M_\infty = 2.0$ and zero angle-of-attack.

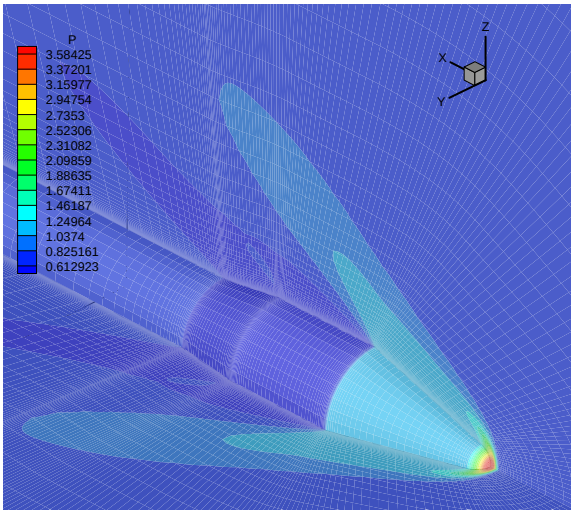

Figure 10: Pressure contours over the vehicle forebody for $M_\infty = 2.0$ and zero angle-of-attack.

authors are initiating large simulations with the adaptive mesh refinement routines in order to obtain better resolution of the flow features such as shock waves and expansions. Furthermore, the authors are working in the implementation of a turbulence model to adequately represent the flow physics at the Reynolds numbers of interest for such applications and, therefore, to be able to compare the simulations with the experimental data.

5. Acknowledgements

The authors would like to acknowledge Fundação de Amparo à Pesquisa do Estado de São Paulo, FAPESP, which provides a graduate scolarship for the first author, and Conselho Nacional de Desenvolvimento Científico e Tecnológico, CNPq, which partially supported the project under the Integrated Project Research Grant No. 522413/96-0.

6. References

Anderson, W. K., Thomas, J. L., and Van Leer, B., 1986, Comparison of Finite Volume Flux Vector Splittings for the Euler Equations, "AIAA Journal", Vol. 24, No. 9, pp. 1453–1460.

Azevedo, J. L. F. and Korzenowski, H., 1998, Comparison of Unstructured Grid Finite Volume Methods for Cold Gas Hypersonic Flow Simulations, "Proceedings of the 16th AIAA Applied Aerodynamics Conference", AIAA Paper No. 98-2629, Albuquerque, NM.

Chakravarthy, S. R., 1983, Euler Equations–Implicit Schemes and Boundary Conditions, "AIAA Journal", Vol. 21, No. 5, pp. 699–706.

Jameson, A., Schmidt, W., and Turkel, E., 1981, Numerical Solution of the Euler Equations by Finite Volume Methods Using Runge-Kutta Time-Stepping Schemes, "Proceedings of the AIAA 14th Fluid and Plasma

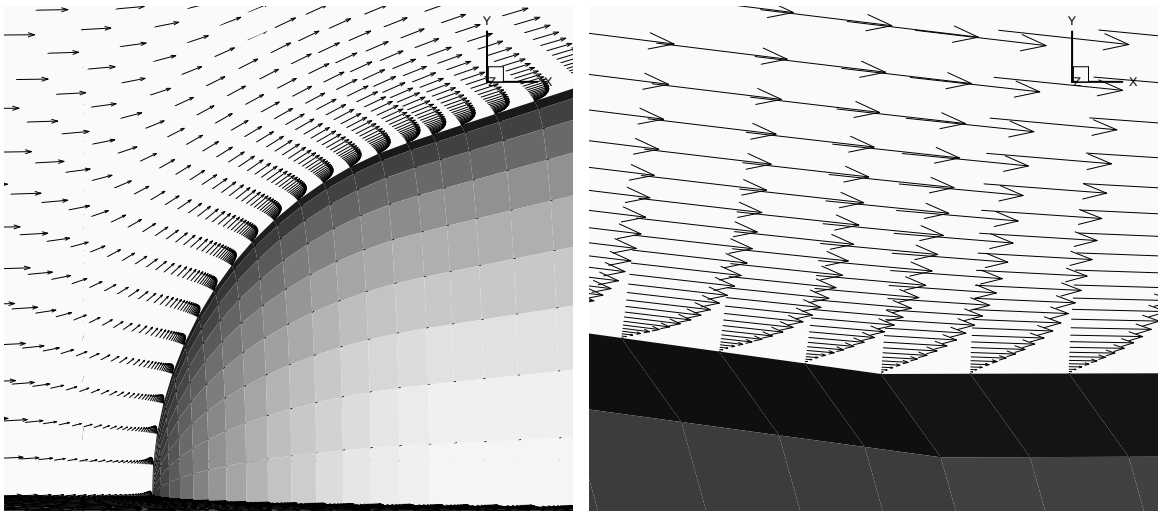

(a) Vehicle nose cap region.

(b) Boattail region.

Figure 11: Velocity profiles over the VLS for $M_\infty = 2.0$ and zero angle-of-attack.

Dynamics Conference", AIAA Paper No. 81-1259, Palo Alto, CA.

Long, L. N., Khan, M., and Sharp, H. T., 1991, A Massively Parallel Euler/Navier-Stokes Method, "AIAA Journal", Vol. 29, No. 4.

Mavriplis, D. J., 1988, Multigrid Solution of the Two-Dimensional Euler Equations on Unstructured Triangular Meshes, "AIAA Journal", Vol. 26, No. 7, pp. 824–831.

Mavriplis, D. J., 1990, Accurate Multigrid Solution of the Euler Equations on Unstructured and Adaptive Meshes, "AIAA Journal", Vol. 28, No. 2, pp. 213–221.

Scalabrin, L. C., Azevedo, J. L. F., Teixeira, P. R. F., and Awruch, A. M., 2002, Three Dimensional Flow Simulations with the Finite Element Technique over a Multi-Stage Rocket, "Proceedings of the 40th AIAA Aerospace Sciences Meeting and Exhibit", AIAA Paper No. 2002–0408, Reno, NV.

Steger, J. L. and Warming, R. F., 1981, Flux Vector Splitting of the Inviscid Gasdynamic Equations with Application to Finite Difference Methods, "Journal of Computational Physics", Vol. 40, No. 2, pp. 263–293.

Strauss, D. and Azevedo, J. L. F., 1999, A Numerical Study of Turbulent Afterbody Flows Including a Propulsive Jet, "Proceedings of the 17th AIAA Applied Aerodynamics Conference", pp. 654–664, Norfolk, VA.

Van Leer, B., 1982, Flux-Vector Splitting for the Euler Equations, "Lecture Notes in Physics", Vol. 170, pp. 507–512.